Available online at www.sciencedirect.com
ScienceDirect
International Journal of Heat and Mass Transfer 51 (2008) 2784–2800
International Journal of HEAT and MASS TRANSFER
www.elsevier.com/locate/ijhmt

An improved model for two-phase hydrogen flow dynamics

James Pasch [a,*], Samim Anghaie [b,c,1]

[a] 2720 Whistler Lane, Hampton Cove, AL 35763, USA
[b] Nuclear and Radiological Engineering, University of Florida, P.O. Box 116502, University of Florida, Gainesville, FL 32611-6502, USA
[c] Innovative Nuclear Space Power and Propulsion Institute, University of Florida, P.O. Box 116502, University of Florida, Gainesville, FL 32611-6502, USA

Received 23 February 2007; received in revised form 15 September 2007
Available online 26 November 2007

Abstract

Two-phase boiling hydrogen pressure drop is studied in the context of high velocity upflow in a constant, high heat flux, steady state, internal pipe flow environment. The approach of this analysis is to reverse-engineer the best available data to determine mass quality, void fraction, and velocity slip. This is accomplished by applying a one-dimensional, five-equation model, with pressure gradient being the one combined equation. The resulting velocity slips are correlated for high and low pressure conditions. Good agreement is achieved between the pressures predicted using the slip correlations and the measured pressures. Results are in general significantly better than those from the homogeneous equilibrium model.

Keywords: Hydrogen; Two-phase; Convective; Pressure; Experimental; Film boiling

1. Introduction

This paper presents an improved model of the dynamics of two-phase hydrogen flowing inside a highly heated duct. Using the best available data, an approach to improve the prediction capabilities for pressure drop is presented. Accurate predictions of pressure drop in a pipe during forced convective two-phase flow benefit engineers throughout the life of a product. During the design phase, a good pressure drop model will help the engineer reduce the uncertainty in the design parameters. During the product test and development phase, good models will help the engineer to correctly interpret test data, therefore allowing him to determine where modifications are necessary. Problems inevitably arise that require a root cause investigation. This requires a good understanding of how the product will react under off-nominal operating conditions. An accurate model allows the engineer to perform this investigation with confidence that the thermal-hydraulics – related results of the investigation are valid.

The rocket industry uses liquid hydrogen as a fuel. Heat transfer to two-phase flowing hydrogen routinely occurs during three phases of rocket operation; propellant tank filling, rocket engine conditioning, and during rocket firing – usually during the start and shutdown transients. Both liquid propulsion and nuclear thermal propulsion (NTP) systems use hydrogen. Hydrogen is the only viable propellant for the NTP systems because of its low molecular weight that generates the highest specific impulse (Isp) at the maximum operating temperatures of these reactors. The evolution of hydrogen flow in the system involves two-phase flow and heat transfer under subcooled, saturated, and superheated thermodynamic conditions. In addition to rockets, a nascent industry that may require modeling of this sort is the hydrogen-fueled car industry.

This paper presents results from a number of objectives. First, it is necessary to conduct a literature search to determine the best battery of two-phase hydrogen tests to analyze. Using the data from this test series, the next

* Corresponding author. Tel.: +1 256 534 3736.
E-mail addresses: james.j.pasch@nasa.gov (J. Pasch), anghaie@ufl.edu (S. Anghaie).
[1] Tel.: +1 352 392 8653.

0017-9310/$ - see front matter © 2007 Elsevier Ltd. All rights reserved.
doi:10.1016/j.ijheatmasstransfer.2007.09.033

Nomenclature

A	area
A_s	surface area
b	y-intercept of line
C_0	drift flux model distribution parameter
D	diameter
f	friction factor
f_1	low pressure slip correlating parameter
f_2	high pressure slip correlating parameter
G	mass flux
G_0	reference mass flux
g	gravity
h	mass-specific enthalpy
j	superficial velocity
L	length
m	slope of line
p	pressure
q''	heat flux
q''_0	reference heat flux
Q	heat flow rate
r	radial direction, radial distance
Re	Reynolds number
s	velocity slip
t	time
T	temperature
u	velocity
w	mass flow rate
x	mass quality
x_{eq}	equilibrium quality
z	elevation

Greek symbols

α	void fraction
β	volumetric quality
ΔT	temperature differential
χ	Lockhart–Martinelli parameter
ϕ	friction multiplier
μ	viscosity
ρ	density
σ	surface tension, Stefan–Boltzmann constant
τ	shear stress
υ	specific volume

Subscripts

av	average
b	bulk
c	cross section
CL	centerline
crit	critical condition
exp	experimental
f	film conditions
h	hydraulic
i	inlet, interface
int	y-intercept
l	liquid phase
lo	all fluid flowing as liquid
m	mean conditions
rad	radiation
s	saturated conditions
slope	slope
tt	turbulent–turbulent liquid–vapor phases
TP	two-phase
v	vapor phase
w	wall

objective is to evaluate the quality of these data. The nature of the flow regimes must be determined. This controls the approach to model development. Since very high wall to bulk temperature ratios can reasonably be expected with liquid hydrogen flowing in a heated pipe, the effect of radial temperature variation will necessarily be included. This goal will include the generation of void fraction, quality, and slip information that must be evaluated against data. A slip model is proposed that reproduces the correlated data very well, and predicts the pressure drop of other hydrogen data better than the homogeneous equilibrium model. The primary objective is to improve the accuracy of predicted pressure drop of two-phase hydrogen in a forced convection, highly heated, internal pipe flow environment. From the literature search, no extensive analysis of momentum loss in hydrogen, validated against data, has been published. This paper is the first of its kind in this regard.

2. Description of available data

Core et al. [1] performed experiments with hydrogen. Twenty-seven heat transfer tests with liquid hydrogen flowing through an electrically heated stainless steel test section, 6.35 cm long and 0.213 cm inside diameter, were completed in the series. Each test comprised a number of different steady state conditions, isolating the effect of changing inlet pressure, mass flux, or heat flux. As a result, there are a total of 164 steady state conditions, with two points of heat transfer coefficient measurements each, in the set. Only the inlet pressure was measured, so a pressure loss analysis cannot be compared with data. The authors did not present a theoretical correlation for the heat transfer coefficient. Their primary goal was to evaluate the utility of hydrogen as a regenerative rocket nozzle coolant. This source stands out as the only one that presents wall superheats that are likely to represent transition boiling conditions. While

most experimental results indicate that transition boiling occurs between wall superheats of 5 K and 20 K, the data in this experiment show some superheats between these values. Therefore, these data may represent results from transition boiling. The Core et al. data set includes calculated equilibrium qualities based on pressure and enthalpy. Negative equilibrium qualities were set to zero. Therefore, inlet subcooling is not known.

Wright and Walters [2] experimented with liquid and vapor hydrogen flowing in a 15.2 cm long and 0.635 cm inside diameter heated tube. Most of their 35 steady state liquid hydrogen experiments were pre-CHF, with 11 runs showing wall-to-bulk temperature differences consistent with film boiling. In fact, their data show a marked gap in wall-to-bulk temperature differences between 2.8 K and 22.2 K. Temperature differences between these values were not obtained. This gap is consistent with a transition in flow regime from pre-CHF and CHF conditions to film boiling. They concluded that stable film boiling could occur for wall to bulk temperature differences as low as about 22 K. Test section pressure measurements were not obtained.

Lewis et al. [3] experimented with boiling hydrogen and nitrogen flowing upward in a type 304 stainless steel, electrically heated vertical tube 41.0 cm long and 1.41 cm inside diameter. Critical heat fluxes corresponding to transition to film boiling were determined over a range of flow rates, heat fluxes, and qualities. They noted that the maximum CHF increased with increasing mass flux and decreased as the point of transition occurred farther into the tube. The mass flow rates in these experiments were so low that no measurable pressure drops were observed. Maximum wall superheat of 500 K – far beyond that necessary for film boiling – were obtained.

The data used to validate the model were generated at NASA – Glenn Research Center (formerly Lewis Research Center) and published in two separate technical notes by Hendricks et al. [4,5], NASA TN 765 and NASA TN 3095, in 1961 and 1966, respectively. These data sets will be referred to collectively as the NASA data to distinguish them from other hydrogen experiments, or as the 1961 and 1966 data when the data from the individual reports are discussed. The experiments were performed in support of rocket engine modeling for the US manned space program. Following is an extensive description of these experiments.

3. Experimental description

3.1. Experimental setup

The experimental setup for the two batteries of experiments are similar and presented in Fig. 1. Hydrogen was stored in a large tank and pressurized by gaseous hydrogen to force it through the system. Piping from the tank to the test section and the test section were enclosed in a vacuum environment to eliminate convection heat transfer to the piping and working fluid. The vacuum container was a stainless steel cylinder 38.1 cm in diameter. Heat was generated inside the tube metal by applying a voltage across its length. The power supply for heat generation was external to the vacuumed environment. Therefore, the leads for the voltage supply, along with instrumentation leads, were passed through the wall of the vacuum chamber. The voltage was applied to the heated test section through copper flanges brazed to the tube. It was found that unevenly brazed joints distributed the power unequally circumferentially in the tube. Therefore, multiple connections to the buss bar were made and the brazed joint was X-ray inspected. After passing through the heated test section, the hydrogen was completely vaporized and then exhausted through the roof of the facility into the atmosphere. All system flow conditions were remotely controlled. The system pressure and flow rate were set by valves upstream and downstream of the test section.

Five different tube diameters were used in the NASA experiments, ranging from 0.48 cm to 1.29 cm inside diameter, and all were vertical with hydrogen flowing upwards. The heated test section length in the 1961 and 1966 experiments are 30.5 cm and 61.0 cm long, respectively. Straight, unheated approach lengths were included in all test sections; approximately 12.7 cm for the 1961 tests, and 30.5 cm for the 1966 tests. Approach sections and test sections were contained within the vacuum environment.

All test sections had 12 thermocouples along the outer surface of the heated lengths, plus inlet and exit temperatures in the mixing chambers. Connections to the tube outer wall were made with great care to avoid affecting the test conditions or measurements. Circumferential thermocouple placements were intended to determine the circumferential uniformity of power distribution in the tube and as checks for accuracy.

The 1961 data had five static pressure taps spaced along the length of the test section and one at each of the inlet and exit mixing chambers. These pressure measurements were not differential relative to a datum. The other four tubes from the 1966 experiments had three static pressure taps spaced along the test section, and one at each of the inlet and exit mixing chambers. These pressure measurements were differential relative to the pressure reading just upstream of the test section inlet. To complete the pressure data set, smooth curves were hand-fitted through the measurements. From these curves, pressure values were interpolated at the locations corresponding to the 12 thermocouple measurements.

3.2. Instrumentation

Mass flow rates were measured both upstream and downstream of the test section. A venturi was placed upstream of the test section and a sharp-edged flow orifice was placed downstream of the heat exchanger. A second venturi, primarily used for flow control, was also used for

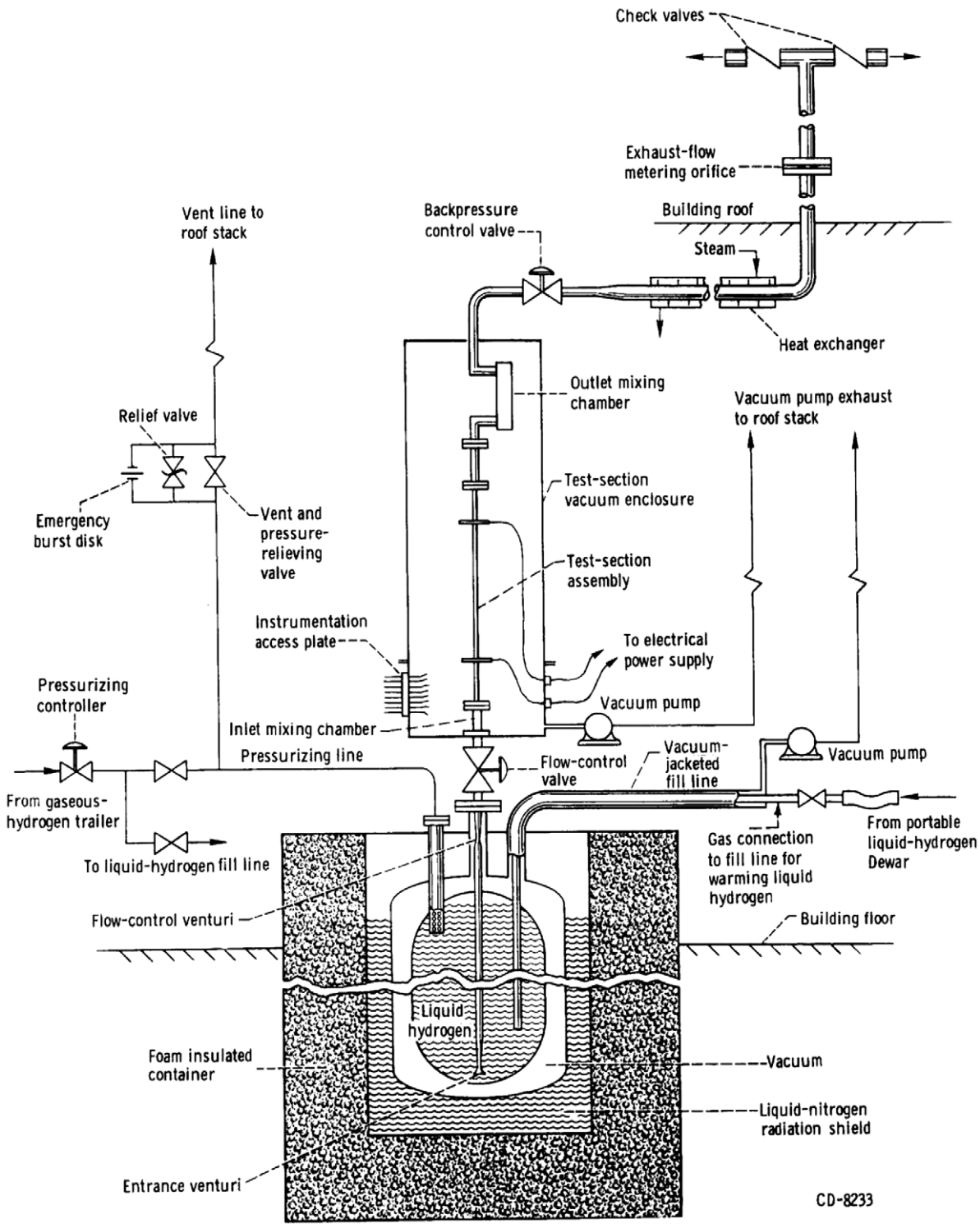

Fig. 1. Experimental setup for hydrogen tests [5].

mass flow measurements. Measurements from these were compared for accuracy, and all agreed to within 3%.

Local values of voltage drops were measured by eight voltage taps along the length of the heated test section to assist in determining local power generation. Two sets of voltmeters and ammeters that had independent shunts or taps were used. These incremental measurements of power input were summed and compared with the overall power input measured by voltage and ammeter taps at the bottom and top of the test section. Agreement between these two methods was good. Accuracies for these measurements are stated to be 1%.

3.3. Experimental conditions

Heat fluxes and mass flow velocities are very high, and tube diameters are similar to those used in regeneratively cooled rocket engine nozzles and other rocket engine piping. The experimental conditions of these data reflect the nature of hydrogen flowing in a rocket engine. Table 1 presents a summary of test conditions. The run numbers listed in this table shall be used to reference specific runs in the data set. Runs 1–31 were generated for the 1966 report, and runs 32–51 were generated for the 1961 report.

Table 1
Table of experimental conditions

Run	G	P_{in}	q''	dp	ΔT_{sub}	D_{inner}
	kg/m^2 s	kPa	kW/m^2	kPa	K	cm
1	327	759	1193	27	−0.1	1.288
2	643	969	948	22	−3.1	1.288
3	329	743	735	15	−0.1	1.288
4	488	1023	768	13	−2.6	1.288
5	662	1045	752	12	−3.8	1.288
6	630	733	719	20	−1.3	1.288
7	873	1075	1324	45	−4.1	1.113
8	536	1103	1308	76	−2.7	1.113
9	895	889	1242	41	−3.3	1.113
10	531	868	817	20	−2.4	1.113
11	1237	616	1357	211	−2.9	0.851
12	1119	861	1324	86	−4.8	0.851
13	892	984	703	32	−6.6	0.851
14	906	982	425	12	−7.2	0.851
15	1553	1251	1766	102	−3.8	0.851
16	1286	1112	1733	113	−2.7	0.851
17	1178	759	2093	250	−2.6	0.851
18	1129	1221	1733	93	−3.3	0.851
19	1121	812	1635	148	−0.2	0.851
20	945	685	1798	201	−1	0.851
21	932	746	2076	223	−0.9	0.851
22	3444	1265	1128	274	−6.6	0.478
23	1965	1141	1112	232	−4.9	0.478
24	2466	1059	1112	272	−6.2	0.478
25	2446	1072	981	272	−6.2	0.478
26	3186	856	670	160	−6.2	0.478
27	2383	823	654	201	−4.3	0.478
28	2735	817	670	146	−5.3	0.478
29	2669	594	294	104	−3.8	0.478
30	3406	613	310	124	−4.6	0.478
31	2165	561	294	109	−2.7	0.478
32	1617	310	376	59	0	0.795
33	1242	279	376	68	0	0.795
34	849	228	376	51	0	0.795
35	575	188	376	38	0	0.795
36	1653	359	621	79	−0.8	0.795
37	1123	311	637	87	0	0.795
38	804	259	637	71	0	0.795
39	1553	399	981	107	−2.4	0.795
40	1242	359	981	103	−1.6	0.795
41	858	303	997	114	−0.2	0.795
42	721	257	997	101	0	0.795
43	1379	448	1144	132	−1.3	0.795
44	1626	457	1357	136	−3.2	0.795
45	1206	399	1373	141	−2.1	0.795
46	849	339	1373	146	−0.7	0.795
47	712	286	1373	126	0	0.795
48	1297	490	1520	149	−2	0.795
49	922	408	1520	153	−0.8	0.795
50	621	335	1520	132	0	0.795
51	1516	498	1651	165	−3.2	0.795

3.4. Data validation

The NASA data are validated by comparing the heat transfer coefficients with other experiments under similar operating conditions. There are 31 tests in the Core et al. [1] experiments with operating conditions similar to NASA runs. The root-mean-squared (RMS) difference in the heat transfer coefficient for these runs is 46%. The Wright and Walters [2] experiments had three similar runs, with a RMS difference of 17%. The Lewis et al. [3] experiments did not have any runs with operating conditions similar to these NASA data for comparison. It is determined from these comparisons that these NASA data are valid.

4. Flow structure analysis

In their flow regime analysis of the 1961 data, Pasch et al. [6] determined that these data are post-CHF. The wall superheat levels and heat transfer coefficient trending of the 1966 data show that these data are, for the most part, post-CHF as well. There are four runs – 22, 26, 29, and 30 – that exhibit wall superheat trending that are consistent with transition from pre- to post-CHF. The wall to bulk delta temperatures are low in the lower portion of the tube. At a certain point for each of these runs, the delta temperature rises dramatically. It is at these points that dry-out occurs. The conclusion from this analysis is that the vast majority of these NASA data are in the film boiling flow regime, with the four runs listed above being the only exceptions.

5. Model development

Film boiling of hydrogen is modeled in this analysis as a separated flow of vapor and liquid. The liquid flows as a homogeneous core through an annulus of homogeneous vapor. In this geometry, the vapor interfaces with both the wall and the liquid core, while the liquid interfaces only with the inner boundary of the vapor annulus. All of the heat from the wall is assumed to be absorbed by the vapor through convection. Radiation of energy to the vapor or directly to the liquid is assumed, and will be shown, to be negligible. Additionally, momentum loss through friction at the wall is largely a function of vapor conditions. This approach is consistent with the experimental observations of Kawaji and Banerjee [7,8]. In their film boiling quench front experiments with water flowing upward in a highly heated quartz tube, bubbles were seldom observed in the liquid core. They concluded that nearly all the vapor generated at the liquid–vapor interface flowed upward in the vapor film. They also found no evidence that the liquid column rewetted the tube wall.

Local static pressures, tube wall temperatures, and voltage drops were recorded. This is enough information for

only a three equation model, also known as a homogeneous equation model (HEM), with mixture mass, momentum, and energy conservation equations. An extensive literature search has not uncovered data-based models for vapor superheat or vapor slip in the flow structure of this analysis. It is likely that these profiles will be unique relative to pre-CHF flows, so that information on vapor superheat and slip from pre-CHF will not apply.

The desired information can be obtained with a one-dimensional, five-equation model, with separate vapor and liquid mass and energy flows, but with one momentum equation. This assumes that the local pressure is the same for both fluids, which is commonly accepted. Completing this model requires closure conditions for two of the following three quantities; vapor mass-specific energy flow, vapor slip, and liquid mass-specific energy flow. Since wall temperatures are part of the data set, it was determined that a closure condition for the vapor energy flow, through quantifying vapor superheat, could be reasonably determined. Neither the liquid heating nor the vapor slip is well understood. It was determined to model the liquid energy state. An analysis supporting this approach is presented later. Modeling the interfacial momentum effects was not necessary for the objectives of this analysis. Including such effects would lead to a two fluid model.

5.1. Magnitude of radiation heating

Heat is transported from the tube inner wall to the hydrogen primarily through convection. However, the large temperature differences experienced in the test series raises the concern that radiative heat transfer from the wall to the vapor and/or liquid hydrogen may be significant. While the exact analysis of radiation heating is complex, a simplified analysis of the worst-case scenario will reveal that radiative heating is at least three orders of magnitude less than convective heating.

Sparrow [9] presented a thorough theoretical analysis of the effect of radiation heating from a tube wall to a vapor/liquid flow in film boiling. His work generated a quantitative criterion by which the relative significance of surface-to-liquid radiation can be determined. A more recent paper by Liao [10], which presents an excerpt of his Ph.D. work, addressed this complicated problem by modeling the liquid core flow as a long inner tube at the center of a long outer tube. The equation for radiation heating he applied to this geometry is

$$q''_{\mathrm{rad}} = \frac{\sigma(T_{\mathrm{w}}^4 - T_{\mathrm{l}}^4)}{\frac{1}{\varepsilon_{\mathrm{l}}} + \frac{1-\varepsilon_{\mathrm{w}}}{\varepsilon_{\mathrm{w}}}\frac{r_{\mathrm{l}}}{r_{\mathrm{w}}}}. \tag{1}$$

The emissivities, ε, that will lead to the largest radiative heating are 1 for both hydrogen and wall. The radiative heat flux then reduces to

$$q''_{\mathrm{rad}} = \sigma(T_{\mathrm{w}}^4 - T_{\mathrm{l}}^4). \tag{2}$$

The highest wall temperature from the data is 560 K, and the fluid temperature is roughly 25 K. Using these values to represent the upper limit of radiative heating, the magnitude is 5.6 kW/m^2. The lowest heat flux in the data set is 294 kW/m^2, several orders of magnitude larger. Additionally, this lowest heat flux does not correspond to the highest wall temperature of 560 K used in this analysis, but instead has a much lower wall temperature of 178 K. In summary, there is no run in this data set that has a radiative heating contribution of more than 2% of the total applied heat flux, and in fact is certainly much less than 2%. The impact of omitting radiative heating of hydrogen in the set of equations is therefore justified.

5.2. Conservation equations

Most of the experimental runs have subcooled liquid entering the heated test section. The amount of subcooling is appreciable, up to 7 K in some runs, and cannot be ignored in the energy balance. The velocities attained in some of the experiments required that the stagnation enthalpies of the two fluids be used in the energy balance instead of the static enthalpies. Thus, the momentum and energy equations are coupled and must be solved simultaneously.

A one-dimensional model of this system was developed to calculate mass, momentum, and energy balances. It is assumed that the pressure is constant across the flow cross-section, and while separate velocities of the two phases are determined, the bulk velocity for each phase is used. Additionally, bulk thermodynamic properties are assumed.

The conservation of mass equation is simply

$$w = w_{\mathrm{l}} + w_{\mathrm{v}}. \tag{3}$$

The liquid momentum equation is

$$\frac{\mathrm{d}}{\mathrm{d}z}(\rho_{\mathrm{l}} u_{\mathrm{l}} A_{\mathrm{c,l}} u_{\mathrm{l}})\mathrm{d}z = -\frac{\mathrm{d}}{\mathrm{d}z}(PA_{\mathrm{c,l}})\mathrm{d}z + \tau_{\mathrm{i}} 2\pi r_{\mathrm{i}}\mathrm{d}z - g\rho_{\mathrm{l}} A_{\mathrm{c,l}}\mathrm{d}z, \tag{4}$$

where τ_{i} and r_{i} are the vapor–liquid interface shear stress and radial location, and A_{c} is the flow area. The corresponding equation for the vapor phase is

$$\frac{\mathrm{d}}{\mathrm{d}z}(\rho_{\mathrm{v}} u_{\mathrm{v}} A_{\mathrm{c,v}} u_{\mathrm{v}})\mathrm{d}z = -\frac{\mathrm{d}}{\mathrm{d}z}(PA_{\mathrm{c,v}})\mathrm{d}z - \tau_{\mathrm{i}} 2\pi r_{\mathrm{i}}\mathrm{d}z - \tau_{\mathrm{w}}\pi D\mathrm{d}z - g\rho_{\mathrm{v}} A_{\mathrm{c,v}}\mathrm{d}z. \tag{5}$$

In a one-dimensional analysis such as this, these separate momentum equations are combined by equating the interfacial interactions of the two phases and solving for the pressure gradient. The result is seen in Eq. (6):

$$-\frac{\mathrm{d}P}{\mathrm{d}z} = \frac{G^2\left\{\frac{\partial x}{\partial z}\left[\frac{-2(1-x)}{\rho_{\mathrm{l}}(1-\alpha)} + \frac{2x}{\rho_{\mathrm{v}}\alpha} + \frac{\partial \alpha}{\partial x}\left(\frac{(1-x)^2}{\rho_{\mathrm{l}}(1-\alpha)^2} - \frac{x^2}{\rho_{\mathrm{v}}\alpha^2}\right)\right] - \frac{x^2}{\rho_{\mathrm{v}}^2\alpha}\left(\frac{\partial \rho_{\mathrm{v}}}{\partial T}\right)_P \frac{\partial T_{\mathrm{v}}}{\partial z}\right\}}{1 - G^2\left[\frac{x^2}{\rho_{\mathrm{v}}^2\alpha}\left(\frac{\partial \rho_{\mathrm{v}}}{\partial P}\right)_T + \frac{(1-x)^2}{\rho_{\mathrm{l}}^2(1-\alpha)}\left(\frac{\partial \rho_{\mathrm{l}}}{\partial P}\right)_T\right]} \times \frac{-\frac{(1-x)^2}{(1-\alpha)\rho_{\mathrm{l}}^2}\left(\frac{\partial \rho_{\mathrm{l}}}{\partial T}\right)_P \frac{\partial T_{\mathrm{l}}}{\partial z} + \tau_{\mathrm{w}}\frac{4}{D} + g[\rho_{\mathrm{l}}(1-\alpha) + \rho_{\mathrm{v}}\alpha]}{1 - G^2\left[\frac{x^2}{\rho_{\mathrm{v}}^2\alpha}\left(\frac{\partial \rho_{\mathrm{v}}}{\partial P}\right)_T + \frac{(1-x)^2}{\rho_{\mathrm{l}}^2(1-\alpha)}\left(\frac{\partial \rho_{\mathrm{l}}}{\partial P}\right)_T\right]}. \tag{6}$$

This equation is similar to that commonly presented in two-phase flow textbooks, but with Jacobian expansions useful for this analysis. The following relation for the wall shear stress was used:

$$\tau_w = \frac{f_l G^2}{2\rho_l}\phi_l^2. \tag{7}$$

As previously stated, the velocities attained in some experiments were high enough that they should be included in the energy balance. Radiation heating of the liquid is omitted based on the previous analysis of liquid heating by radiation. As a result, conservation of energy is modeled as follows:

$$\dot{Q} = wx\left[h_v + \frac{1}{2}\left(\frac{Gx}{\rho_v \alpha}\right)^2\right] + w(1-x)\left[h_l + \frac{1}{2}\left(\frac{G(1-x)}{\rho_l(1-\alpha)}\right)^2\right]. \tag{8}$$

In the application of this equation, the total energy flow rate is determined to be the total energy of the flow at the inlet plus the cumulative energy added through heating:

$$\dot{Q} = w\left[h + \frac{1}{2}u^2\right]_i + q''_w A_s. \tag{9}$$

5.3. Entrance lengths

The developing hydrodynamic and thermal profiles in the vapor from the test section inlet onwards must still be considered. Hsu and Westwater [11] used law-of-the-wall theory to determine that the vapor in the annulus transitions from laminar to turbulent at a $Re = 100$. Computations from Rohsenow et al. [12] for condensation on a vertical plate were used to justify this transition Reynolds number. This transition Reynolds number appears to be commonly quoted and used to determine transition from laminar to turbulent flow of the vapor in film boiling. Note that for typical values of vapor density and viscosity, and for typical velocities at the test section entrance, the vapor annulus dimension that produces a Re of 100 is 0.001 cm – an extremely small thickness. This film thickness is achieved at a void fraction for the smallest tubes in the NASA data set, which will give the largest required void fraction, of 0.008. From this, it is reasonable to assume that the vapor is always turbulent. Additionally, it is hard to conceive of the vapor flowing in a laminar fashion after its violent generation at the heated test section entrance.

As previously discussed, in the tube metal at the boundary between the heated test section and the entrance piping, there will be a significant axial gradient in metal temperature. This will lead to axial heat conduction, which in turn will affect the local heat flux and temperature. Instead of the approximately constant heat flux established within the tube far from the boundaries of the heated test section, the local heat flux can be significantly reduced. Measured wall temperatures from the 0.795 cm diameter tube support this conclusion. It is important to note that, while there is axial heat transfer in the metal, at any particular station near the inlet, all of the energy that is calculated to be transmitted to the flow up to that point will indeed be transmitted to the flow. Thus, the calculated total energy input to the flow up to a given point will not be in error. At the test section exit, this is not the case. Heat flows up and out of the test section at the exit. Thus, the flow will not receive all of the heat input until some point after the heated section exit. The results of an analysis of axial heat transfer on local measured wall temperatures is presented in the data refinement section.

5.4. Closure conditions

To complete the set of equations, the level of bulk vapor superheat, the amount of liquid sensible heating, and the nature of the wall friction must be determined. Vapor superheat was modeled using the following equation:

$$T_m = C(T_s - T_w) + T_w. \tag{10}$$

Various coefficient values were tried between the theoretical 5/6th that applies to a single phase, fully developed turbulent flow with a Prantdl number near one, and the commonly-used 1/2. Energy balance errors were minimized with the smallest coefficient of 1/2. Therefore, it was determined to proceed with this value. This coefficient value is consistent with the analyses of Takenaka et al. [13] in his film boiling studies. Nijhawan et al. [14] performed experiments in which they measured vapor superheats in post-CHF flowing water. They observed significant superheating of the vapor. Their data strongly support the use in this effort of 1/2 for the vapor superheat coefficient.

As stated previously, an assumption must be made regarding the energy state of the liquid. The assumption used in this analysis is that the liquid experiences no sensible heating. It remains at its inlet temperature throughout the heated tube unless the local pressure drops to the saturation pressure for the liquid temperature. From this point onward, the liquid temperature assumes the saturation temperature at the local pressure.

Rationale for this assumption comes from the fact that vapor is definitely present during film boiling, even for subcooled flows. Therefore, the liquid certainly does not absorb and evenly distribute 100% of the energy from the tube wall. That is, the fluid does not increase in temperature to saturation before it starts to generate vapor. This observation easily extends into the saturated condition in which it is logical to assume that a saturated liquid also does not absorb 100% of and evenly distribute the energy input from the wall. The true nature of the liquid heating almost certainly lies between the extremes of no sensible heating and thermodynamic equilibrium.

Using some assumptions, the exact theoretical time-dependent liquid temperature profile as it flows through the core of the tube was solved. The liquid core was modeled as an infinitely long rod of constant radius R having a uniform initial temperature T_l and instantaneously sub-

jected to a uniform temperature bath at temperature T_s. It is assumed that the bath temperature is the saturation temperature of the fluid at the local pressure. That is, any liquid that rises above the saturation temperature evaporates and leaves the liquid core and does not heat the remaining liquid. Only liquid that is at the saturation temperature or lower remains to conduct heat from the liquid/vapor interface inwards. This model also assumes that the liquid is at a uniform temperature across its radius at the initial time heat is applied (the test section inlet), that liquid radial velocity gradients are unimportant to heat transfer, and properties are constant. That is, heat transfer in the liquid can be modeled by conduction alone. Using values for necessary parameters that are typical for these data, it has been determined that the amount of sensible liquid heating is indeed very small – a conclusion that supports the approach in this analysis. This is primarily due to the very short residence time of the liquid in the test section.

The frictional losses are modeled with a Blasius-type relation for the friction factor and a two-phase friction multiplier developed by Rogers [15] at Los Alamos National Lab. His model was developed for friction modeled as only the liquid component of the two-phase flow flowing alone. Thus, the friction factor is

$$f = 0.079 Re_l^{-0.25}. \tag{11}$$

Rogers' model was developed specifically for two-phase internal flow hydrogen. Although his model is largely theoretical with some data validation, it is applicable to the entire two-phase hydrogen pressure range, and is presented in closed form as follows:

$$\phi_f^2 = \left(\frac{1-x}{x}\right)^{1.8} \times \left\{1 + \frac{x^{0.8187}\left[0.1324(12.759-P)+0.03966(12.759-P)^3\right]}{P^E}\right\}, \tag{12}$$

where pressure is in atmospheres, and E is

$$E = 1.896x - 2.646x^2 + 1.695x^3. \tag{13}$$

5.5. Model implementation

During the implementation of this theory, two observations directed the final form of the algorithm. First, implementing the theory requires an iterative scheme with discretized quality and void fractions. Each combination of quality and void fraction will result in errors in predicted pressure drop and energy flow relative to measurement. Acceptable levels of error must be defined, which results in a quality-void fraction pair domain of solutions from which a final pair must be selected. Second, it was found that there are some points for which this model will not simultaneously satisfy both momentum and energy conservation within the targeted small error. This is due mostly to the inaccuracies of the model, and probably to a lesser extent due to inaccuracies in experimental measurements. For most points, momentum and energy conservation are satisfied with negligible errors associated with the necessity of discretization.

It is for these two reasons that 'smart' iteration techniques failed. Several other methods of finding the correct quality-void fraction solution were implemented that relied on reducing the error in energy and momentum by determining the correct direction to change each value. However, these iteration methods were found to be inadequate due to the nature of the equations in the problem and due to the fact that, in some cases, the solution of least error for some points is greater than the target error limits for most other points.

Performing a 'dumb' progression of quality/void fraction pairs, while not conservative of CPU time, was found adequate. Note that the thermodynamic state of the vapor and liquid are known since liquid temperature, vapor temperature (through the superheat equation), and local pressure are known.

The error limits placed on calculated momentum and energy changes are 2% of measurement. All quality-void fraction pairs that agreed with the measured pressure loss to within 2% were saved for processing in the energy balance. This preliminary solution set was then input to the energy balance. The solution domain is constrained by noting the contribution of velocity to the total energy flow. It is significantly less than that of enthalpy even for the high velocity flows. Therefore, the energy balance is a very weak function of void fraction and a very strong function of quality. Thus, the quality range is always reduced to one or a few discretized values, but with a range of void fractions that satisfy the momentum equation within the error limits.

It is logical to use the liquid and vapor velocities to discriminate between the remaining solutions. Various methods were tried. One method required the vapor velocity to be greater than the liquid velocity at all points, but this did not work best for runs near the critical pressure. A slip of less than one appears to satisfy these runs best. Another constraint that led to problems for high pressure runs was to require the vapor velocity to increase monotonically up the tube. It was finally determined to select the minimum vapor velocity from the set of solutions that satisfied the energy balance within the specified error limit. This constraint eliminated extremely high vapor velocities, some well over the sonic velocity, while giving reasonable results for high pressure runs.

To address points for which momentum and energy conservation can not simultaneously be satisfied, it was determined to equally increase the accepted momentum and energy errors until a solution was obtained for both. Note that increasing the acceptable range of errors on momentum consistently decreases the calculated errors in energy balance, so this method found the lowest level of error for both quantities while giving preference to neither.

6. Results

6.1. Data refinement

The NASA data set comprises 51 steady state runs in which there are 12 data points each. It was necessary to generate another point at the test section inlet in order to initialize the algorithm. Thermodynamic conditions at the inlet were approximated by using homogeneous equilibrium theory and subtracting the heat input from the inlet to the first published point. Therefore, for all runs, the first point is at the heated test section inlet. For runs 1–31, the 13th point is 6.3 cm before the heated test section exit. For runs 32–51, the 13th point is at the heated test section exit. The runs fall naturally into five groups based on tube inner diameter. These five tubes will be referred to as tubes 1 through 5, in order of run numbers listed in Table 1.

It was determined through various means that the data set needed to be refined. The points that are affected by inlet and exit effects, and any calculations that include these affected points, should be excluded from analyses. For runs 1–31, point 1 at the test section inlet falls into this category. Only results between point 2 at 6 cm and point 13 at 55 cm will be considered. For runs 32–51, points 1, 2, and 13 at the inlet, 0.1 cm, and at the test section exit will be excluded. Only results between point 3 at 1.6 cm and point 12 at 29 cm will be considered. Fig. 2a presents the wall temperature profiles for runs 35, 38, 42, and 47. Evident in these runs are the end effects in which heat is conducted axially within the tube metal at the inlet and exit of the test section. The steep gradient in wall temperatures for most runs between points 2 and 3 at 0.14 cm and 1.5 cm at the inlet and points 12 and 13 at 29 cm and 30.5 cm prove the end effect. What is of particular interest are the runs in which the inlet and exit temperatures are actually higher than their adjacent measured temperatures inward from the ends. This indicates that there is an end effect other than axial heat conduction influencing measured wall temperatures. This can be explained by considering that the collars brazed onto the test section ends to apply a voltage will not distribute the current absolutely evenly across the tube metal radius. The current flow will distribute itself across the thickness of the metal over a finite distance, and will be concentrated near the brazed collar at the ends. Therefore, the current density will be higher at the tube outer wall where the collar is brazed and will therefore generate more heat towards the outer part of the wall, where the thermocouple is attached.

The pressure data exhibited uneven trending, to varying degrees, in all runs. This unevenness can present problems for a modeling algorithm using the pressure data to solve for other flow conditions. Therefore, a smooth regression line was generated for each run to represent the axial pressure profile. It was found that a third order least squares fit modeled all runs very well, with correlation coefficients very near unity for most runs.

There are some data whose validity is called into question. The basis for questioning these points lies in apparent discontinuities between adjacent values. Run 42 point 8 at 19 cm, presented in Fig. 2a, shows a rise in wall temperature of 40–50 K at the 18 cm elevation relative to adjacent wall temperatures. This magnitude of temperature rise and fall over a 7 cm length, and the fact that the event is exceptional in these data, begs an explanation. A similar effect is evident in run 32 at 27 cm. It may be that a unique flow structure occurs for a short length in these runs. The computer model is robust enough to accommodate many, but not all, of these changes and solve for the momentum and energy balances within the specified limits.

For some points in which the wall temperature increases drastically from the previous point, the model cannot satisfy the energy balance. This is because of the assumption that all vapor at a point is at the calculated mean vapor temperature, which is a function of the wall temperature. If there is a large increase in wall temperature, then the increase in mean vapor enthalpy may require a larger energy addition than the energy added through heating from the previous point, even with zero additional vaporization. That is, even if all the energy from heating were used to heat the vapor instead of generating more vapor, the increase in enthalpy still would be less than that calculated using the mean vapor temperature. To satisfy these points, the quality would have to be reduced, which is assumed to not be possible in the model. This is why these

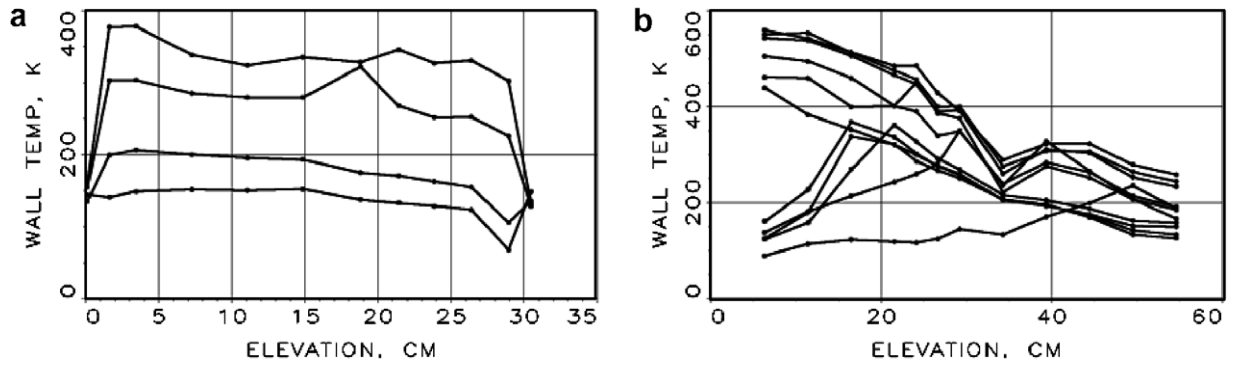

Fig. 2. (a) End effects evident at inlet and exit for runs 35, 38, 42, 47. (b) A consistent wall temperature decrease occurs at the 34 cm elevation in tube 3.

points of high increase in wall temperature are consistently associated with negative energy addition errors – the measured added energy can not attain the increase is vapor energy.

Tube 3 exhibits a consistent decrease in wall temperature at the 34 cm location. Fig. 2b presents the wall temperatures for all 11 runs on tube 3. This is interpreted as a bias in the measurement. Therefore, in making calculations using the wall temperature, these experimental values have been replaced by a linear interpolation between adjacent points. The only other wall temperature point that was deemed obviously out-of-family was run 42, at the 19 cm elevation. This point also was replaced by a linear interpolation between adjacent points. While other points in the data set showed erratic trending, it was usually uncertain which points should be modified. A common characteristic is for adjacent points to trend oppositely, e.g., one low and the next high. Which point was biased was usually not determined. Therefore, no modifications were made.

Tube 4 runs, 22–31, have by far the highest mass fluxes in the database. This is likely the reason that four of these runs exhibit low wall temperatures in the lower portions of the test section. As discussed previously, these runs are associated with pre-CHF conditions and therefore will be excluded from consideration. Two other runs, 28 and 31, produce bad energy balances. Thus, four runs (23, 24, 25, and 27) remain from tube 4. These remaining four runs were excluded from the correlation process since the nature of their test conditions and resulting slips are removed from the general body of data.

Four other runs (14, 32, 36, 44) are excluded based on their generally higher energy and momentum errors. Also, run eight has proven to be difficult to process for all variants of the model attempted. This analysis has failed to explain its pressure profile. While there are occasional momentum and energy balance errors in other runs, it has been determined that useful information can be obtained from them. Therefore, all other runs will be considered further. Thus, after excluding pre-film boiling runs, bad momentum and energy balance runs, and runs with bad void profiles, there remains a total of 36 runs and 398 points of measurement for further consideration.

6.2. Model results

The processing of data from these runs does not generate perfect results. Momentum balance within 10% of measurement is achieved in all but 10 instances, and to with 5% of measurement for all but 20 points. Energy balance is achieved within 10% of measurement in all but 11 cases, and to within 5% of measurement for all but 44 cases. The great majority of incremental pressure drops and energy additions for each run are well modeled. Momentum and energy balances that fall outside the targeted 2% variance from measurement are typically caused by steep changes in wall temperatures, as previously discussed. In these cases, the calculated quality does not change from one point to the next, in order to minimize the energy addition error.

Fig. 3a presents the resulting void profiles from the model for the runs that will be included in the correlation process. In general, the void profiles for the remaining 36 runs rise steeply but smoothly. Discontinuities are in general caused by steep changes in wall temperatures. Fig. 3b presents the resulting velocity slip ratios from the model for the culled data set. The trend of the slip profiles are in general smooth.

6.3. Validation of model results

Fig. 3a shows that an extremely steep void fraction build-up occurs in film boiling, and departs markedly from the relatively shallow build-up predicted by models such as that resulting from the Lockhart–Martinelli parameter. These results are consistent with findings of Per Ottosen [16] in which void profiles in film boiling conditions were measured using γ-ray scattering. Ottosen published the first known results from the use of γ-ray absorption to measure void fraction in low velocity film boiling nitrogen. He observed the transition from inverted annular film boiling to dispersed film boiling at void fractions between 80% and 90%. Rohsenow and coworkers [17–19] used nitrogen in their studies of film boiling. In their work, they determined the actual mass quality. They observed that the transition from inverted annular film boiling to dispersed film

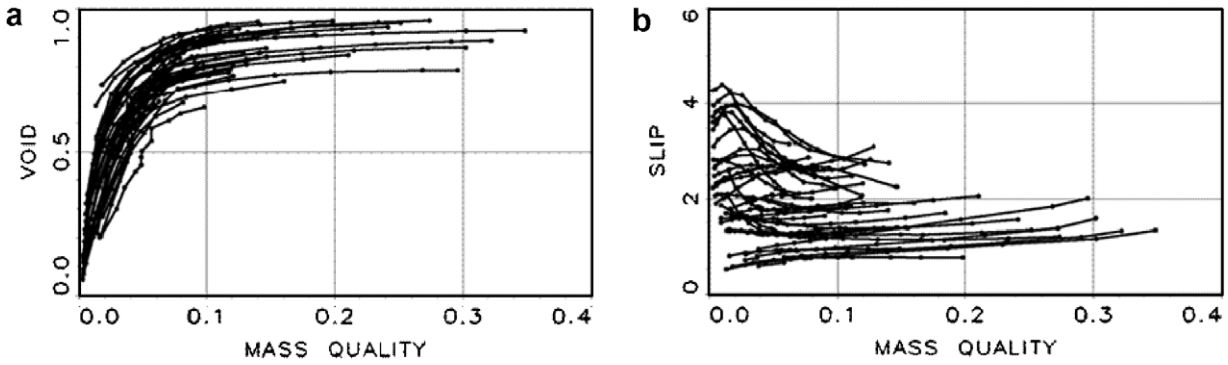

Fig. 3. Calculated void fraction (a) and slip ratio (b) vs. quality from model for the culled data set.

boiling occurred at a mass quality of about 10%. Combining this observation with Ottosen's of the void fraction at transition, it can be concluded that void fractions of 80–90% at a mass quality of 10% are typical. These experimental observations agree well with the results of this model.

7. Data correlation

There remain 36 runs from which a correlation can be obtained. This gives 398 points, and 362 momentum and energy balances for the effort. The mass fluxes range from approximately 300 kg/m^2 s to 1600 kg/m^2 s, the pressure range is from 180 kPa to the critical pressure, heat flux ranges from approximately 370 kW/m^2 to 2100 kW/m^2, with four different tube diameters, and two different tube lengths.

Three different approaches were attempted to correlate the pressure drop data. First was the attempt to correlate the resulting void fraction profiles. As Fig. 3a shows, the 36 runs kept for analyses had a relatively tight grouping of void fractions.

The fact that the void fraction profiles for all 36 runs grouped together rather tightly presents a difficulty in trying to correlate the data. No good parameter for discriminating between two different runs with similar void profiles yet with significantly different operating conditions was found. While some success was achieved with a correlating parameter composed of heat flux, mass flux, and density ratios, the results were much less than desirable. Therefore, the attempt to directly correlate the void fraction data as a function of known parameters was abandoned.

Next, the theory of the drift flux model was applied. In this theory, void fraction is modeled as

$$\alpha = \frac{\beta}{C_0 + u_{gj}/j}. \tag{14}$$

The volumetric quality, β and superficial velocity, j, are known functions of mass flux, quality, and liquid and vapor densities. This leaves the distribution parameter, C_0, and vapor drift velocity, u_{gj}, to be determined for void fraction to be predicted.

Of the correlations reviewed, C_0 is typically between 1.0 and 1.3 for most flow conditions. As Zuber and Findlay [20] pointed out, C_0 can be below 1.0 when the void fraction is higher near the wall than near the centerline – an uncommon condition in most pre-critical heat flux flow regimes. However, this is the fundamental nature of film boiling.

While correlations exist for C_0 and u_{gj}, most of them are based upon a relatively well-mixed flow of liquid and vapor. The vapor is concentrated near the center of the pipe. As such, these correlations typically capture the physics of buoyancy effects. Ishii [21] presented many correlations related to drift flux theory, none of which pertain to film boiling. The literature search did not reveal any formulation or correlation that predicts the drift flux terms for separated, high velocity vertical flow with vapor along the wall. Klausner et al. [22] recommended a value of 0.98 for C_0 and 1.12 m/s for u_{gj} in pre-CHF annular vertical upflow. These values were used in the analysis of Fu and Klausner [23] that resulted in good predictions of pressure drop and heat transfer in this flow regime. These values were also applied to the NASA data. Results show that the predicted slip for all points lay between 0.34 and 1.16, with negative slopes for all runs. While these slip predictions are better for some runs relative to the slip correlation of this paper, most slips are better predicted by the new model presented in this paper.

The standard method of correlating the distribution parameter and the vapor superficial velocity was used. The ratio of vapor superficial velocity to void fraction was plotted against the mixture superficial velocity. A family of curves resulted, the slopes and y-intercepts of which give C_0 and u_{gj}. The slopes vary around unity, giving distribution parameter values for most points between 0.6 and 1.2. The vapor drift velocity was observed to vary a significant amount from run to run, and not in an obvious trend. It was concluded that there may be a better way to correlate these data than to develop separate correlations for both the vapor superficial velocity and the distribution parameter.

The third approach to correlating the data attempted to predict the velocity slip ratio, defined as

$$s = u_v/u_l. \tag{15}$$

Fortunately, this variable varied within an adequate range for the 36 runs, as shown in Fig. 3b. Not only does the level of slip vary to a reasonable degree, but so too did the variation as a function of quality.

A literature search for slip and void fraction correlations has revealed numerous published models. A variety of these were applied to these NASA data. Unfortunately, no slip correlation specifically developed for film boiling was found. Table 2 presents the accuracies of these correlations at predicting the slip. It is observed that none of these models predict the slip very well. Thom [24] correlation performed the best, with an 81% prediction accuracy to with 50% of this model's slip. His model is based on work with boiling water.

As a result of the inability of the published correlations to model these data, it was determined to develop a slip correlation. Several different approaches were used to develop a correlating parameter for slip. First, a mechanistic relation of the vapor and liquid velocities was pursued by applying law-of-the-wall concepts. The goal of this approach was to develop a relation for the velocity ratio that allowed the interfacial conditions to cancel out. Using some rather weak assumptions, a transcendental relation for film thickness and flow conditions was derived. It was found that the interfacial velocity would not cancel out in a velocity ratio since it is an additive term to the interfacial vapor velocity.

As a result of this finding, the search for a correlating parameter shifted to trying various combinations of

Table 2
Results of various slip and void fraction models applied to the NASA data

Slip model source	Accuracy to within					Model
	10%	20%	30%	40%	50%	
Pasch & Anghaie	47%	78%	91%	95%	98%	
CISE (Premoli, [25])	6%	16%	31%	44%	57%	$s = 1 + e1\sqrt{\frac{y}{1+ye2} - ye2}$ $e1 = 1.578\left(\frac{GD}{\mu_l}\right)^{-0.19}\left(\frac{\rho_l}{\rho_v}\right)^{0.22}$ $e2 = 0.0273\left(\frac{G^2D}{\sigma\rho_l}\right)\left(\frac{GD}{\mu_l}\right)^{-0.51}\left(\frac{\rho_l}{\rho_v}\right)^{0.08}$ $y = \left(\frac{\rho_l}{\rho_v}\right)\left(\frac{x}{1-x}\right)$
Smith [26]	12%	25%	34%	43%	51%	$s = e + (1-e)\sqrt{\frac{\frac{\rho_l}{\rho_v} + \left(\frac{1-x}{x}\right)}{1+e\left(\frac{1-x}{x}\right)}}$ $e = 0.4$
Bankoff [27]	7%	12%	17%	23%	28%	$\alpha = \frac{0.7}{1 + \left(\frac{\rho_v}{\rho_l}\right)\left(\frac{1-x}{x}\right)}$
Chisholm [28]	12%	23%	34%	43%	52%	$s = \sqrt{1 - x\left(1 - \frac{\rho_l}{\rho_v}\right)}$
Zivi [29]	1%	3%	6%	8%	12%	$s = \left(\frac{\rho_l}{\rho_v}\right)^{1/3}$
Klausner [22]	4%	15%	27%	39%	52%	$\alpha = \left[C_0\left(1 + \left(\frac{1-x}{x}\right)\left(\frac{\rho_v}{\rho_l}\right)\right) + u_{gj}\frac{\rho_v}{Gx}\right]^{-1}$ $C_0 = 0.98$ $u_{gj} = 1.12$
Ahrens [30]	8%	26%	36%	54%	65%	$s = \left(\frac{\mu_l}{\mu_v}\right)^{0.2}$
Wallis [31]	1%	2%	2%	4%	4%	$\alpha = \left[1 + \left(\frac{1-x}{x}\right)^{0.72}\left(\frac{\rho_v}{\rho_l}\right)^{0.40}\left(\frac{\mu_l}{\mu_v}\right)^{0.08}\right]^{-1}$
Lockhart & Martinelli [32]	16%	31%	43%	57%	67%	$\alpha = \left[1 + 0.28\left(\frac{1-x}{x}\right)^{0.64}\left(\frac{\rho_v}{\rho_l}\right)^{0.36}\left(\frac{\mu_l}{\mu_v}\right)^{0.07}\right]^{-1}$
Zuber & Findlay [20]	12%	23%	33%	44%	51%	$C_0 = 1.2$ $u_{gj} = 1.53\left(\frac{g\sigma(\rho_l - \rho_v)}{\rho_l^2}\right)^{0.25}$
Coddington [33]	16%	26%	36%	51%	64%	$C_0 = 2.57E - 3P + 1.0062$ $u_{gj} = (6.72E - 7P^2 - 8.81E - 5P + 1.05E - 3)G + 5.63E - 3P^2 - 0.123P + 0.8$
Thom [24]	16%	30%	57%	71%	81%	$\alpha = \left[1 + \left(\frac{1-x}{x}\right)^{1.0}\left(\frac{\rho_v}{\rho_l}\right)^{0.89}\left(\frac{\mu_l}{\mu_v}\right)^{0.18}\right]^{-1}$
Baroczy [34]	12%	25%	37%	46%	55%	$\alpha = \left[1 + \left(\frac{1-x}{x}\right)^{0.74}\left(\frac{\rho_v}{\rho_l}\right)^{0.65}\left(\frac{\mu_l}{\mu_v}\right)^{0.13}\right]^{-1}$

parameters representing test conditions, and various exponents on these parameters. As previously stated, it was observed that the slip very near a quality of zero and the slope of the slip as a function of quality varied. These observations led to attempting to develop a correlation that predicted the initial slip (near zero quality) and the slope of the slip as a function of quality. Each of these two components was modeled as a linear function of a correlating parameter.

To pursue this approach, the slip profiles for the 36 runs were modeled as linear functions of quality. From this, 36 slip slopes and slip y-intercepts were generated. In turn, the 36 values of each of these two variables were modeled as functions of the correlating parameter, henceforth called

the slip factor, f. Ostensibly, a different slip factor could be generated for the 36 y-intercepts and the 36 slopes, each used in a linear model to predict the initial slip and the slip slope.

Due to the no-slip condition at the wall, the inception of vapor generation should correspond to a slip of zero. The zero velocity liquid next to the wall is the first liquid to be vaporized, and this vapor will have zero velocity. This fact is not evident in Fig. 3b. It appears that the various slips will extrapolate to finite values at a quality of zero. Probably the source for this discrepancy lies in the form of the wall friction model used in the pressure drop calculation. The Blasius equation is used, which is based on law-of-the-wall theory, but is intended for use on a large scale, not for use when the bulk of the vapor would be better modeled by near-wall physics. In addition, the validity of law-of-the-wall theory probably deteriorates when the film thickness is extremely thin. The liquid–vapor interface acts as a second wall to alter the physics from that which is modeled by the Blasius equation.

Regardless, the value of the slip can be extrapolated from the straight line representing each slip curve to a quality of zero, and this family of 36 slips can be correlated. The effect on gross calculations such as pressure drop are minimal, since the void fraction is truly small very near the inlet, whether the slip is modeled as zero at a quality of zero or if it is finite. As void accumulates, the Blasius equation becomes more accurate, so the error in modeling the physics is reduced. The detrimental effect on determining the nature of pressure drop is self-mitigating.

A routine of nested Fortran "do loops" was constructed to optimize the specific dimensionless ratios and their respective exponents that make up the slip factors. A typical trial slip factor might look like the following:

$$f = \left(\frac{\mu_l}{\mu_v}\right)^a \left(\frac{P_{in}}{P_{crit}}\right)^b \left(\frac{G}{G_0}\right)^c \left(\frac{q''}{q''_0}\right)^d \left(\frac{L}{D}\right)^e. \tag{16}$$

The nested do loops iterated through each exponent, over the range from -2.0 to $+2.0$, in 0.2 increments so that 20 different values of each exponent were tried. Therefore, five nested do loops would generate 20^5 or 3.2 million correlating parameters, each to be statistically compared with the 36 y-intercept values and the 36 slope values.

In the initial application of this method, it was found that the aspect ratio term, L/D, tended towards a very large exponent to optimize the correlation. It was determined that the optimizing algorithm tended towards this large aspect ratio exponent – easily approaching 5 if allowed – in an attempt to accommodate the variation in slip between the 1961 data and the 1966 data, in which the lengths are 0.305 m and 0.61 m, respectively. This variation in slip could be a result of experimental differences. In addition, the extremely limited variation in tube length in the database does not warrant including a tube length effect. Therefore, it was determined to generate separate slip correlations for the 1961 (low pressure) and 1966 (high pressure) data sets.

7.1. Low pressure slip correlation

Within this framework, it was observed that the 1961 data could still be well modeled by the original slip y-intercept and slip slope method previously discussed. However, this method did not work well for the 1966 data. The correlation coefficients were too low to support this approach. Instead, it was determined that the 1966 data slip profiles could be better modeled as a constant along the length of the tube for each run, but varying for each run. This approach is similar to the work of Rigot [35], in which he used an average slip value of 2 for his application.

Taking the 1961 data, for each combination that made up the trial slip factor, a linear least squares analysis was performed on both the y-intercept fit and the slope fit, with the correlation coefficients (R^2) returned for each fit to determine the goodness. Thus, to optimize the fits of the y-intercepts and the slopes, there will be two slip factors, each one with two coefficients used in a linear slip formula. The y-intercepts and slopes will look like the following equations:

$$\text{slip intercept} = m_{int}(f_{int}) + b_{int}, \tag{17}$$

$$\text{slip slope} = m_{slope}(f_{slope}) + b_{slope}, \tag{18}$$

where for the slip y-intercept, m_{int} and b_{int} are the slope and y-intercept, and for the slip slope, m_{slope} and b_{slope} are the slope and y-intercept. f_{int} and f_{slope} are the slip y-intercept and slip slope factors, hence forth called the intercept slip factor and the slope slip factor.

The following ratios were tried: liquid to vapor viscosity, liquid to vapor density, mass flux to an average mass flux G_0 (1000 kg/m^2 s), heat flux to an average heat flux q''_0 (1000 kW/m^2), reduced inlet pressure (to the critical pressure). Note that for the high system pressure correlation analysis, an aspect ratio of tube length to tube diameter was included.

It was found that non-linear effects were involved. That is, the optimum exponent on one ratio is affected by the presence or absence of another ratio, and their associated exponents. Also, it was found that the sensitivity of the goodness of fit varied for different ratios. From this analysis, it was determined that the viscosity and mass flux ratios were not important. Therefore, they were eliminated from subsequent analyses.

It was also found that the intercept slip factor and slope slip factor were optimized using the same grouping of terms with very nearly the same exponents. The best exponent for the heat flux ratio differed slightly for the intercept and slope slip factors. Thus, with only a small degradation in accuracy, a single slip factor, f_1, can be defined that predicts the slip y-intercept and slope.

The equations for the y-intercept and slope were determined to be

$$\text{slip intercept} = -5.20 + 1.12 f_1, \tag{19}$$

$$\text{slip slope} = (103 - 14.9 f_1)x, \tag{20}$$

where x is the mass quality, and the slip factor is defined by

$$f_1 = 4.0E3 \left(\frac{P_{in}}{P_{crit}}\right)^{-1.8} \left(\frac{q''}{q''_0}\right)^{1.2} \left(\frac{\rho_l}{\rho_v}\right)^{-1.8}. \tag{21}$$

The correlation coefficients are 0.82 and 0.71 for the slope and y-intercept, respectively. These equations can easily be combined to produce the correlating equation for slip:

$$s = (103 - 14.9 f_1)x - 5.20 + 1.12 f_1. \tag{22}$$

The test section inlet pressure range over which this correlation applies is up to 500 kPa. Note that the slip factor is not a function of local conditions, and is calculated at the inception of film boiling. This is because the slip throughout a run is modeled as a linear function of quality. The slope and y-intercept of the slip are determined at the inception of film boiling.

7.2. Low pressure slip correlation assessment

The low pressure correlating parameter shows that the initial slip decreases as system pressure increases, increases as applied heat flux increases, and decreases as the liquid to vapor density ratio increases. The pressure and density effects seem to be contradictory. Higher system pressures correspond to a lower liquid to vapor density ratio, which normally corresponds to lower slip, which is in direct contradiction to the density ratio effect in the slip factor. However, these dependencies must be interpreted in light of the set of parameters included in the optimizing algorithm. Vapor superheat was not explicitly included in the slip factor optimization algorithm. Therefore, if local vapor superheat is truly an influence, then its effect will be accounted for through another parameter that correlates with superheat, such as the density ratio. Therefore, the density ratio is likely a surrogate parameter for the effect of superheat on parameters such as vapor viscosity. Isolating the effect of the density ratio, an increase in this parameter is caused by a decrease in vapor density, which in turn is caused by higher vapor temperatures. This also will lead to higher vapor viscosity, and thus, higher friction and lower vapor velocity. Over a short distance, the liquid velocity does not have time to change, so a reduction in vapor velocity will lead to a reduction in slip. The range of viscosity variation is a factor of roughly 3.5 in these data, which is fairly significant, as a result of the variation in vapor superheat.

The pressure parameter is interpreted to account for the density effect. As described above, higher system pressures decrease the liquid to vapor density ratio. The acceleration each phase experiences is directly a function of their densities and pressure gradient. Since both phases are subject to the same pressure gradient, the variation in density ratio will control the variation in slip. Thus, higher system pressures should decrease slip. This is consistent with the trend in the slip correlation factor.

The initial slip increases with heat flux. The pressure gradient also increases consistently with heat flux. As pressure gradient increases, the effect on slip near the inlet will be to increase it, as described above. The significantly lighter vapor will be accelerated much more than the denser liquid. Thus, slip will increase. Therefore, the heat flux parameter represents the effect of the pressure gradient.

7.3. High pressure slip correlation

The high system pressure correlation is simpler since the slip is being modeled as a constant. The slip is correlated with an R^2 value of 0.72 with the following equation:

$$s = 2.88 f_2 - 1.37. \tag{23}$$

In this, the correlating parameter f_2 is modeled as

$$f_2 = \left(\frac{\rho_l}{\rho_v}\right)^{0.3} \left(\frac{\mu_l}{\mu_v}\right)^{0.8} \left(\frac{L}{D}\right)^{-0.4}. \tag{24}$$

The tube inlet pressure range over which this correlation applies is from 600 kPa to the critical pressure (1284 kPa). Note that there is still an aspect ratio effect, but that the exponent is optimized at a much lower value than if the 1961 and 1966 data were combined. This dependence reflects the influence of the three different tube diameters on the data.

7.4. High pressure slip correlation assessment

Eq. (24) shows that the high pressure slip increases with increasing liquid to vapor density ratio, increasing liquid to vapor viscosity ratio, and decreasing aspect ratio L/D. The density ratio effect here is interpreted the same way as the pressure ratio effect in the low pressure slip factor. The acceleration each phase experiences is directly a function of their densities and pressure gradient. Since both phases are subject to the same pressure gradient, the variation in density ratio will control the variation in slip. Thus, increasing the liquid to vapor density ratio will increase slip. The liquid to vapor viscosity ratio probably is at least partially a surrogate for the effects of vapor superheat, just as the density ratio was for the low pressure data. The viscosity ratio shows that, as vapor viscosity decreases, the slip will increase – a physically reasonable effect. Finally, the effect of the aspect ratio L/D shows that slip increases as this ratio decreases. This can be interpreted in terms of the difference between the absolute film thickness relative to the void fraction as tube diameter varies. Comparing a small and large diameter tube, the film thickness will be larger for the large diameter tube than for the small diameter tube for the same void fraction. Thus, the average velocity of the vapor with the larger film thickness will be higher.

7.5. Accuracy of the slip correlations

The accuracy of these two correlations at reproducing the model slips are presented in tabular form in Table 2.

Results show that excellent agreement is achieved. The slip correlation can now be used in the model to directly solve for the pressure drop. Instead of iteratively solving for the quality and void fraction pairs that best fit the data, the slip as a function of system parameters and local quality can be used to calculate the local slip and subsequently the void fraction. In this application as applied to a particular length segment, properties are a function of the segment inlet pressure and the average vapor temperature across the length segment.

The quality of the slip correlation is assessed by comparing predicted and measured pressure drops. For the 1961 data there are nine pressure drop increments per test that are unaffected by end effects, and 17 tests included for a total of 153 pressure drop increments. For the 1966 data there are 11 acceptable increments per test and 19 tests for a total of 228 increments. Thus, there are 362 pressure drop increments to compare. Accuracy is determined here in terms of the percentage of incremental pressure drops that are predicted to within a specified percentage of experimental pressure drops.

Fig. 4 presents the accuracy of predicted versus measured pressure gradients. The dashed lines represent plus and minus 30% from the measured pressure gradient. All data used to generate the slip correlation are included in this plot. The majority of positive error points correspond to the extremely high pressure runs of 15, 16, and 18. This model predicts 42% of the data to within 10% compared with the HEM accuracy of only 12%. For 30% accuracy, this model predicts 81% of the data compared with the HEM results of 37%. At 50% accuracy, predictions from this model encompass 89% of the data compared with 56% for the HEM.

Improved accuracy is obtained by using mass quality instead of equilibrium quality. The HEM pressure profiles frequently have a knee, in which the pressure profile slope is shallow, followed by a significantly steeper region. The knee is the point at which equilibrium quality changes from negative to positive. This point is further discussed later.

Some of the lowest pressure runs show that the HEM predicts a pressure loss that would generate a negative pressure. That is, HEM is incapable of predicting pressure in these cases.

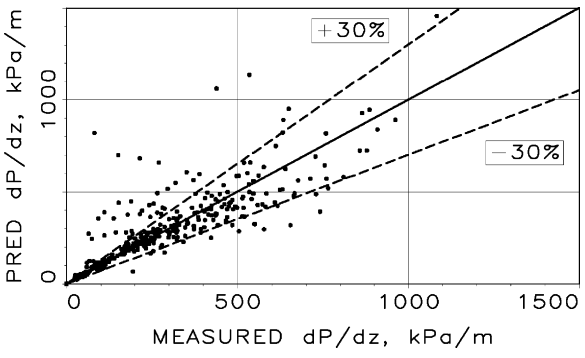

Fig. 4. Predicted versus measured pressure gradients for all data used in correlating slip.

7.6. Validation of the slip correlations

The slip correlations are validated by comparing predicted and measured pressure profiles for runs that were excluded from the correlation process. Fig. 5 presents four plots of measured and predicted pressure profiles of runs that were excluded from the correlation process; runs 32, 36, 44, and 23. The measured profile in each plot is the solid line with circles, the prediction from this model is the long dashed with squares, and the HEM prediction is the short dashed with diamonds. In runs 32, 36, and 44, presented in Fig. 5a–c, this model performs extremely well – much better than the HEM predictions. However, for the very high mass flux runs on tube 4, represented by run 23 in Fig. 5d, this model does not perform well, and the HEM does significantly better at reproducing the pressure profile. This analysis shows that the model developed here performs extremely well, but for a limited mass flux range.

The comparison of pressure profiles for run 39 in Fig. 6a shows the limitations of the HEM at predicting the pressure profile while the flow is subcooled, from a thermodynamic equilibrium standpoint. The slope of the HEM pressure profile prediction is very shallow while equilibrium quality is negative. It is not until equilibrium saturation is achieved at the 11 cm elevation that the HEM prediction becomes more accurate. This characteristic shortcoming of the HEM pressure predictions is consistently observed throughout the pressure range of these NASA data. Since this model uses mass quality and accounts for non-equilibrium effects, its predictive accuracy is not reduced in subcooled conditions. The data show that the concept of equilibrium quality is not relevant, and this model reflects this fact.

The model is particularly less accurate at extremely high system pressures. Runs 15, 16, and 18 are the three highest system pressure runs in the dataset, and the proposed model consistently performs less well for these three runs than for any other runs in the culled dataset. Fig. 6b is representative of these three runs. The subcooled equilibrium state of the flow is evident in the HEM pressure predictions, and in general, the HEM profile does not reflect the trending of the data. The predicted profile of this model does reflect the general trend of the data, but the predicted accuracy is worse than for lower pressure runs.

The ranges of validity of the two correlations should be listed separately. The low pressure correlation is valid from pipe inlet conditions of 180–500 kPa, mass fluxes from approximately 580 kg/m^2 s to 1650 kg/m^2 s, and heat fluxes from approximately 380 kW/m^2 to 1650 kW/m^2. The high pressure correlation is valid for pipe inlet conditions of 600 kPa to the critical pressure, mass fluxes from approximately 330 kg/m^2 s to 1550 kg/m^2 s, and heat fluxes from

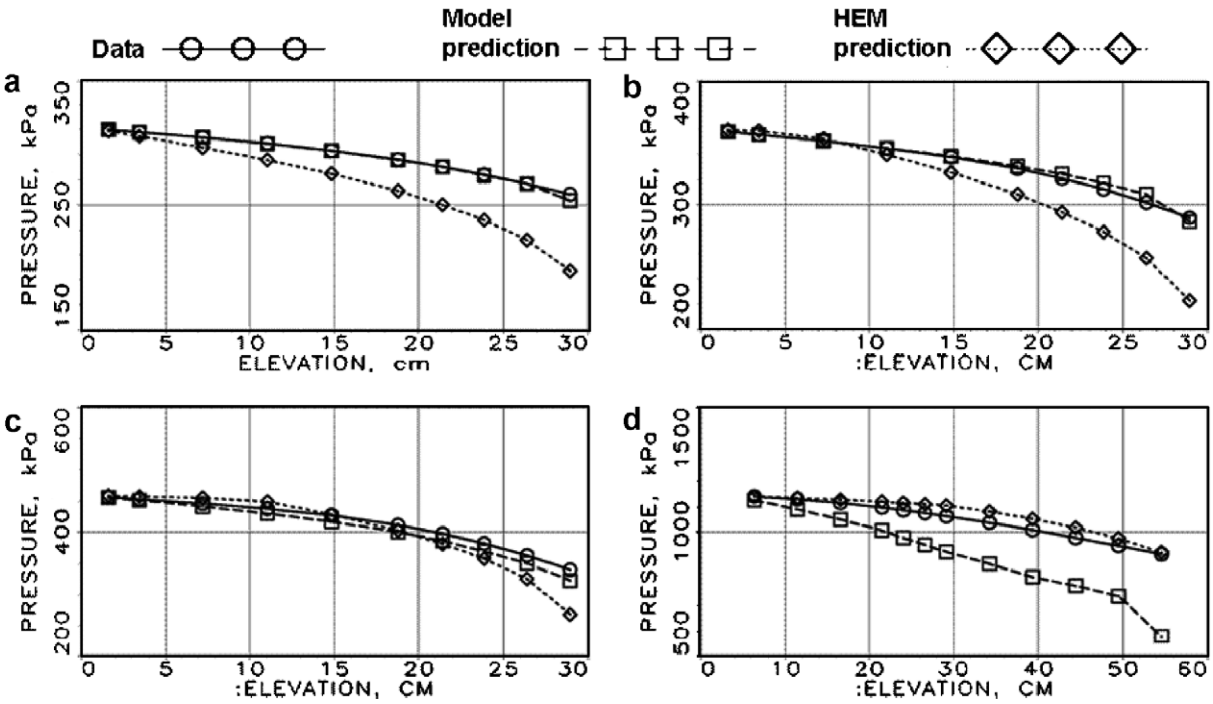

Fig. 5. Measured and predicted pressure profiles for run 32 (a), 36 (b), 39 (c), and 23 (d), which were excluded from the correlation generation data set.

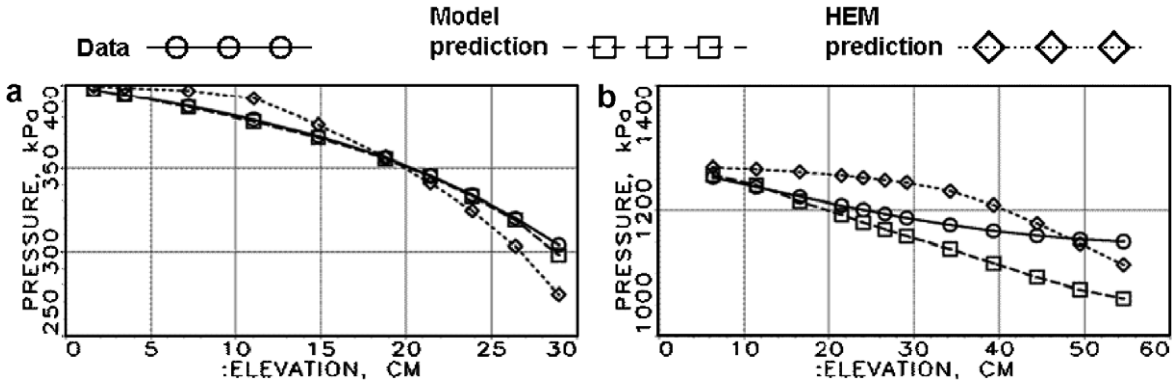

Fig. 6. (a) Run 39 and (b) run 15 measured and predicted pressure profiles.

approximately 700 kW/m^2 to 2100 kW/m^2. For inlet pressures between 500 kPa and 600 kPa, it is recommended to use the lower pressure correlation.

8. Observations

The high pressure slip model can predict the pressure profile with good accuracy even for length segments for which the energy balance was not well satisfied. These are seen in the figures as points in which slip and void change value while the quality remains constant. The high pressure model does not appear to work well for all extremely high pressure runs. The highest pressure runs, 15, 16, and 18, are not well reproduced, particularly in the upper half of the tube. However, other high pressure runs, such as 4, 5, and 7, are reasonably well modeled. This model performed poorly for the highest mass flux runs on tube 4. For very high mass fluxes, it is recommended to use the HEM model.

The low pressure correlation performs very well, in general. Runs that are less well predicted tend to be those that have a low mass flux to heat flux ratio. However, the runs that were excluded from the correlation optimization process are quite well reproduced.

The slip correlations and this momentum and energy balance model provide for a method in which pressure drop can be accurately predicted regardless of the subcooled nature of the flow. The knees observed in the HEM greatly limit its usefulness in the subcooled region. The assumption of no significant liquid heating (all heated liquid is vaporized), and initializing quality at zero at the inlet appear to be reasonable approximations.

Acknowledgement

The authors wish to express their gratitude to Robert Hendricks for giving freely of his memories of these experiments in which he was centrally involved. His efforts, then and now, provide the engineering community with unique and valuable information.

References

[1] T.C. Core, J.F. Harkee, B. Misra, K. Sato, Heat transfer studies, WADD TR 60-239, Aerojet-General Corporation, Wright Air Development Center, September, 1959.
[2] C.C. Wright, H.H. Walters, Single tube heat transfer tests – gaseous and liquid hydrogen, WADC TR 59-423, Wright Air Development Center, August, 1959.
[3] J.P. Lewis, J.H. Goodykoontz, J.F. Kline, Boiling heat transfer to liquid hydrogen and nitrogen in forced flow, NASA TN D-1314, Lewis Research Center, September, 1962.
[4] R.C. Hendricks, R.W. Graham, Y.Y. Hsu, R. Friedman, Experimental heat transfer and pressure drop of liquid hydrogen flowing through a heated tube, NASA TN-D-765, May, 1961.
[5] R.C. Hendricks, R.W. Graham, Y.Y. Hsu, R. Friedman, Experimental heat-transfer results for cryogenic hydrogen flowing in tubes at subcritical and supercritical pressures to 800 pounds per square inch absolute, NASA TN-D-3095, March, 1966.
[6] J. Pasch, M. Popp, S. Anghaie, Flow regime analysis of forced flow boiling hydrogen subjected to high heat flux, ASME Heat Transfer Conference 2005, July 17–23, 2005, San Francisco, CA. Paper HT2005-72453.
[7] M. Kawaji, S. Banerjee, A two-fluid model for reflooding of a vertical tube: structure and stability of the inverted annular flow model, Am. Inst. Chem. Eng. Symp. Ser. 79 (225) (1983) 236–249.
[8] M. Kawaji, S. Banerjee, Application of a multifield model to reflooding of a hot vertical tube: part 1 – model structure and interfacial phenomena, J. Heat Transf. 109 (1987) 204–211.
[9] E.M. Sparrow, The effect of radiation on film-boiling heat transfer, Int. J. Heat Mass Transf. 7 (2) (1964) 229–238.
[10] J. Liao, Modeling two-phase transport during cryogenic chilldown in a pipeline, PhD dissertation, University of Florida, Department of Mechanical and Aerospace Engineering, 2005.
[11] Y.Y. Hsu, J.W. Westwater, Approximate theory for film boiling on vertical surfaces, Chem. Eng. Prog. Ser. 56 (1960) 15–24.
[12] W.M. Rohsenow, J.H. Webber, A.T. Ling, Trans. Am. Soc. Mech. Eng. 78 (1956) 1637.
[13] N. Takenaka, T. Fujii, K. Akagawa, K. Nishida, Flow pattern transition and heat transfer of inverted annular flow, Int. J. Multiphase Flow 15 (5) (1989) 767–785.
[14] S. Nijhawan, J.C. Chen, R.K. Sundaram, E.J. London, Measurement of vapor superheat in post-critical-heat-flux boiling, J. Heat Transf. 102 (1980) 465–470.
[15] J.D. Rogers, Two phase friction factor for para-hydrogen between one atmosphere and the critical pressure, AIChE J. 14 (6) (1968) 895–902.
[16] P. Ottosen, An experimental and theoretical investigation of inverse annular film flow and dispersed droplet flow, important under LOCA conditions, RISO-R-424, Riso National Laboratory, DK 4000, Roskilde, Denmark, July, 1980.
[17] R.S. Dougall, W.M. Rohsenow, Film boiling on the inside of vertical tubes with upward flow of the fluid at low qualities, 9079-26a, Massachusetts Institute of Technology, Department of Mechanical Engineering, September, 1963.
[18] W.F. Laverty, W.M. Rohsenow, Film boiling of saturated nitrogen flowing in a vertical tube, J. Heat Transf. 89 (1967) 90–98.
[19] R.P. Forslund, W.M. Rohsenow, Dispersed flow film boiling, J. Heat Transf. 90 (1968) 399–407.
[20] N. Zuber, J.A. Findlay, Average volumetric concentration in two-phase flow systems, J. Heat Transf. 87 (1965) 453–468.
[21] M. Ishii, One-dimensional drift-flux model and constitutive equations for relative motion between phases in various two-phase flow regimes, ANL-77-47, Argonne National Laboratory, October, 1977.
[22] J.F. Klausner, B.T. Chao, S.L. Soo, An improved method for simultaneous determination of frictional pressure drop and vapor volume fraction in vertical flow boiling, Experim. Therm. Fluid Sci. 3 (1990) 404–415.
[23] F. Fu, J.F. Klausner, A separated flow model for predicting two-phase pressure drop and evaporative heat transfer for vertical annular flow, Int. J. Heat Fluid Flow 18 (1997) 541–549.
[24] J.R.S. Thom, Prediction of pressure drop during forced circulation boiling of water, Int. J. Heat Mass Transf. 7 (1964) 709–724.
[25] A.F. Premoli, A.D. Prina, An empirical correlation for evaluating two-phase mixture density under adiabatic conditions, paper B9, European Two Phase Flow Group Meeting, Milan, Italy, 1970.
[26] S.L. Smith, Void fractions in two-phase flow. A correlation based on an equal velocity head model, Proc. Inst. Mech. Eng. 184 (36) (1969) 647–664.
[27] S.G. Bankoff, A variable density single fluid model for two-phase flow with particular reference to steam-water flow, J. Heat Transf. 82 (265) (1960).
[28] D. Chisholm, Two-Phase Flow in Pipelines and Heat Exchangers, George Godwin of Longman Group Limited, New York, 1983.
[29] S.M. Zivi, Estimation of steady-state steam void-fraction by means of the principle of minimum entropy production, J. Heat Transf., Ser. C 86 (1964) 247–252.
[30] F.W. Ahrens, Heat pump modeling, simulation and design, heat pump fundamentals, in: J. Berghmans (Ed.), Proceedings of the NATO Advanced Study Institute of Heat, Pump Fundamentals, Espinho, Spain, The Hague, Netherlands, 1983.
[31] G.B. Wallis, One-Dimensional Two-phase Flow, McGraw-Hill Book Company, New York, 1969.
[32] R.W. Lockhart, R.C. Martinelli, Proposed correlation of data for isothermal two-phase, two-component flow in pipes, Chem. Eng. Prog. 45 (1) (1949) 39–48.
[33] P. Coddington, R. Macian, A study of the performance of void fraction correlations used in the context of drift-flux two-phase flow models, Nucl. Eng. Des. 215 (3) (2002) 199–216.
[34] C.J. Baroczy, Correlation of liquid fraction in two-phase flow with applications to liquid metals, Chem. Eng. Prog. Symp. Ser. 61 (57) (1965) 179–191.
[35] G. Rigot, G., Fluid capacity of an evaporator in direct expansion, ORNL-TR-5217, Oak Ridge, TN., 1973.